Tribology International 181 (2023) 108319

Contents lists available at ScienceDirect

Tribology International

journal homepage: www.elsevier.com/locate/triboint

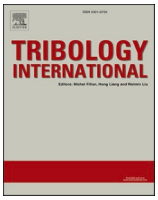

Loading on a wind turbine high-speed shaft gearbox bearing: Ultrasonic field measurements and predictions from a multi-body simulation

B.P. Clarke [a,*], G. Nicholas [a], E. Hart [b], H. Long [a], R.S. Dwyer-Joyce [a]

[a] The University of Sheffield, UK
[b] The University of Strathclyde, UK

ARTICLE INFO

Keywords:
In-situ measurement
Model
Rolling element bearings
Ultrasound

ABSTRACT

Wind turbine gearbox failures, many of which result from load-driven rolling element bearing failures, account for long downtimes and high maintenance costs. Non-invasive, in-situ measurement of bearing roller loads using ultrasound facilitates better understanding of the load history and failure mechanisms these gearbox bearings experience. In this study, ultrasonic load measurements from an instrumented high-speed shaft bearing were compared against results from a static multibody simulation. Measurements taken under steady operating conditions were found to agree well with the model. After quantification of the error in ultrasonic measurements the model enabled identification of load outliers which were attributed to transient events. Over- and under-loading instances may act to promote a variety of failure mechanisms, leading to premature bearing failure.

1. Introduction

Rolling bearings in wind turbines are subject to highly variable loading due to the transient nature of wind, various operational conditions, and the complex system dynamics. Gearboxes in wind turbines have had some of the highest failure rates, resulted in the largest amount of downtime [1] and have been amongst the costliest components to repair [2]. Most gearbox failures have stemmed from failure of bearings, particularly high-speed shaft (HSS) bearings [3], although there is a lack of more modern statistics. Other problematic bearings are main bearings [4,5] and pitch bearings [4,6].

Amongst gearbox bearing failures, a high proportion is attributed to axial cracking, thought to be induced by white etching cracks (WECs) [7,8]. WECs are a widespread network of cracks with microstructural changes observed within the vicinity of the cracks which would appear white if nital etched. Despite WECs being a subject of intensive research, its formation mechanisms are still widely debated. Theories of WEC initiation include non-metallic inclusions [9,10], hydrogen embrittlement [11] and frictional energy dissipated within the contacts through roller slip [12,13]. Alternatively, Manieri et al. [14] provided convincing evidence of bearing load driven WEC formation. Their findings indicated that the high stresses which the bearing experiences early in service results in the initiation of cracks, which under subsequent lower stresses propagates relatively slowly. The white etching area formed is then a consequence of subsequent rubbing of these crack faces. This theory has also been supported by past research [15–18]. Since WECs are widely observed in prematurely failed wind turbine bearings, this has brought into question our understanding of the loading [19] to which these bearings are subjected to in the field.

While some rolling bearing applications are well understood, significant uncertainties remain with respect to their application in wind turbines [5,20–25]. Concerted research efforts are therefore ongoing across a broad range of topics. Central to this is the development of a clear understanding of the true load characteristics experienced by rolling bearings in these machines [21,26–29], which in turn assist in the identification of possible underlying damage mechanisms. To-date these efforts have largely relied on model-based analyses at various levels of fidelity.

Whilst there exist a multitude of ways to predict loading on wind turbine transmission components [29–35], laboratory and field measurements are scarce and have proven to be challenging. A notable exception is from NREL, where strain gauges were used to monitor high-speed shaft bearing loads on a full scale 750 *kW* drivetrain test platform [36]. The method involved machining slots in the bearing raceways for instrumentation. To calibrate the strain gauges, a custom test jig was necessary for recording of strain measurements across a range of known loads. Measurements were taken under various conditions, including normal operation, generator misalignment, simulated

* Correspondence to: Mappin Building, Mappin Street, Sheffield S1 3JD, UK.
E-mail address: ben.clarke@sheffield.ac.uk (B.P. Clarke).

https://doi.org/10.1016/j.triboint.2023.108319
Received 31 October 2022; Received in revised form 15 January 2023; Accepted 31 January 2023
Available online 3 February 2023

braking, and grid loss events. The load distribution around the instrumented bearing circumference was successfully measured. The authors reported that misalignment was found to have little effect on the bearing loading and slip was observed during simulated braking. During the instance of grid loss, torque reversals were identified as the bearing loaded zone shifted. SKF also have the Sensor Roller [37] which replaces one or more of the rollers in bearing and can measure load through the roller. Information on the sensors used for load monitoring and example of data from these sensors is not currently available.

Another recent approach for measurement of bearing load is through using ultrasonic reflectometry. The technique involves sending an ultrasonic wave across the bearing raceway and capturing the signal reflected from the raceway surface. The reflected wave contains information on both the lubrication [38–41] and load [42] at the interface. Lubrication is inferred through amplitude changes of the reflected signal whilst load is inferred through the time-of-arrival change. The time-of-arrival change is a result of a reduction in signal transmission path as the raceway deflects under load. As such, the time-of-flight change can be used to infer raceway deflection and subsequently roller and bearing load through Hertzian contact models. The method has been investigated in a laboratory setting [42] and has also recently been extended to a bearing in an operational wind turbine [43]. The ultrasonic technique clearly holds promise to bridge the gap in measurement and understanding of load in wind turbine bearings.

This work expands on existing analyses of an ultrasonically measured dataset from an operational wind turbine [43,44]. Specifically, we look at the variation in load measurements and account for error from the ultrasonic technique which has not previously been addressed. We use a static multibody model (SABR) to provide further insight into ultrasonic measurements of bearing load and identify instances of transient loading, as well as put the error into context of typical load in wind turbine bearings. We look at load variation between rollers with the new context of measurement error and also analyse load distribution in an operational wind turbine bearing for the first time.

2. Background

As part of a project with the Department of Energy and Climate Change (DECC) UK, instrumentation was carried out on a 600 *kW* Vestas V42 wind turbine located in Donegal, Ireland. This activity was part of a larger project named “OWDIn” [45] led by Ricardo Innovations that included measures to extend the life of planet bearings. Table 1 shows the specifications of the wind turbine whilst Fig. 1 summarizes the sensors installed, where the measurements used for this study originated from. The instrumentation was comprised of two condition monitoring systems (CMS), namely CMS1 and CMS2. CMS1 measurements include generator voltage and current as well as wind speed measurements from the anemometer on the nacelle roof. Voltage sensors and Rogowski coils were employed for measurement of the three phases of generator voltage and current, respectively. CMS2 measurements refer to ultrasonic measurements obtained from the high-speed shaft (HSS) gearbox tapered roller bearing.

The HSS is driven by the rotor, via the gearbox. For this asynchronous fixed-speed pitch-regulated turbine the shaft rotational speed is maintained at its set point via generator torque control at below-rated wind speeds, and by pitch control at above-rated wind speeds. The value of fixed rotational speed at which the turbine operates is selected in order to maximise power capture while avoiding structural harmonics, the aerodynamic stall front and generator operational limits.

Table 1
Vestas V42 turbine specifications.

Wind Turbine	Vestas V42 Fixed-speed pitch control
Rated power (kW)	600
Cut-in wind speed (m/s)	4
Rated wind speed (m/s)	16
Cut-out wind speed (m/s)	25
Rotor diameter (m)	42
Hub height (m)	50
Generator	Asynchronous

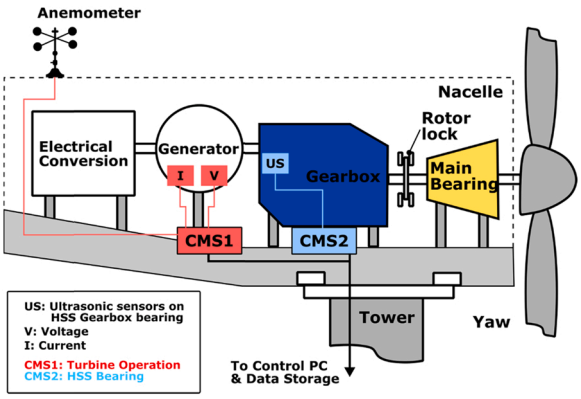

Fig. 1. Overview of condition monitoring systems installed within the wind turbine
(adapted from [46]).

2.1. Generator voltage, current and wind speed instrumentation

Fig. 2 shows the wind mast, Rogowski coils and voltage sensors installed to measure wind speed, generator current and voltage. The voltage sensors were fitted over all 3 phases of voltage terminal bolts whilst Rogowski coils looped around each of the three phases of the current terminals.

2.2. Ultrasonic sensor instrumentation

As HSS gearbox bearings account for a large proportion of failed bearings [3], it was desired to instrument and monitor one of the HSS bearings. Opportunity for instrumentation was made possible when the gearbox was taken out for routine maintenance along with installation of Ricardo’s MultiLife$^{(TM)}$ system [48] for planetary bearings. This allowed access to the HSS bearings. Upon preliminary analysis using a multi-body modelling platform (SABR developed by Ricardo PLC), the most highly loaded pair of the tapered roller bearings was identified (Bearing B) and chosen for instrumentation. The selected bearing was a 32222 tapered roller bearing. Fig. 3(a) shows the location of the bearing relative to other components within the gearbox.

For generation of ultrasound, bare piezoceramic crystals were used. The full process of instrumenting piezoelectric crystals onto bearing raceway surface has been previously detailed in [43] and thus will be omitted here. Two ultrasonic sensors were instrumented on the outer bore of the tapered roller bearing outer raceway. Modification to the outer raceway surface (shown in in Fig. 3(b)) was necessary for two reasons; to accommodate the sensors and cabling and, to ensure that the ultrasonic waves are perpendicularly incident to the roller-raceway surface. The latter was to enable the maximum amount of ultrasonic energy to be reflected back and subsequently captured by the sensor. An image of the instrumented sensors can be seen in Fig. 4(a). The circumferential location of the two ultrasonic sensors were selected based upon where the bearing loaded zone was situated, drawing information from multi-body modelling conducted. One sensor (CH1) was instrumented at the edge of the maximum loaded region (92% of peak load), whilst the other (CH2) at the centre of the maximum loaded region (98% of peak load). Fig. 4(b) illustrates the circumferential positioning of the ultrasonic sensors.

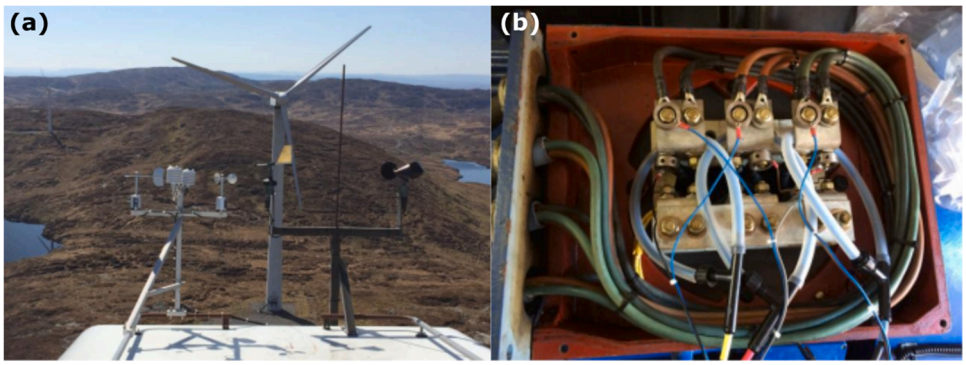

Fig. 2. (a) Anemometer for wind speed measurements and (b) Rogowski coils and voltage sensors fitted to each of the three phases of current and voltage [47].

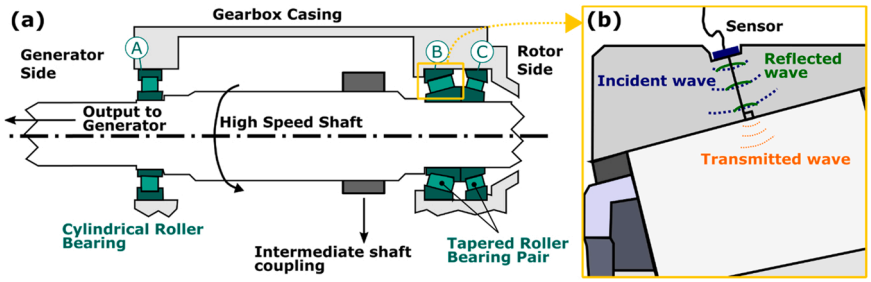

Fig. 3. (a) HSS bearing configuration and (b) requirements for ultrasonic waves to strike the roller-raceway interface perpendicularly. (adapted from [46])

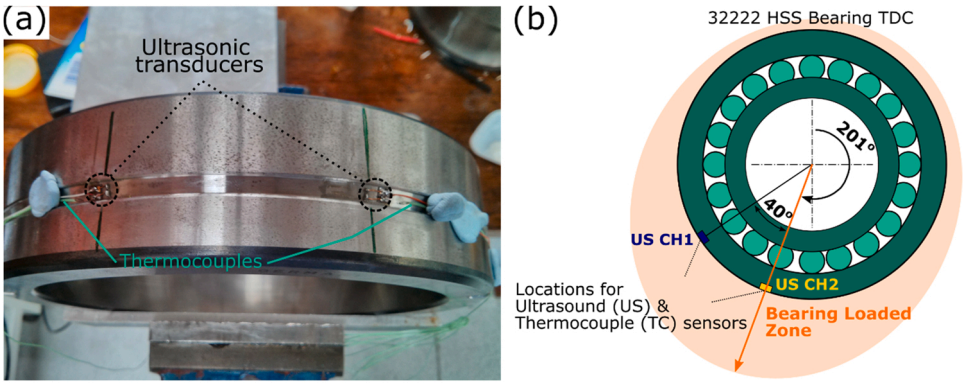

Fig. 4. (a) Photo of the instrumented bearing and (b) radial locations of ultrasound transducers on the instrumented bearing. Angles are defined from top dead centre (TDC).

2.3. Data acquisition

Table 2 summarizes the data acquisition duration and rate of the instrumented sensors. Generator voltage and current were captured at 10.24 *kHz* for 60 s, every minute. Wind speed measurements on the other hand were captured continuously at a lower sampling rate of 50 *Hz*. For the ultrasonic measurements, due to the high sampling rate of 100 *MHz*, measurements were captured only for 1 s at a sensor excitation rate of 80 *kHz* every 20 min. This produced 50 *MB* of data from each of the ultrasonic sensors.

3. Measurement principles

3.1. Generator current, voltage, and wind speed

Fig. 5 shows a sample of the voltage and current measurements for all 3 phases measured through the voltage and Rogowski coil sensors. To calculate the power of each phase, P_{phase}, the alternating voltage and

Table 2
Summary of data acquisition duration and rate.

Data	Number of sensors	Sample duration	Units	Capture rate	Sampling rate
Generator voltage	3	60 *s*	V	Every 1 min	10.24 *kHz*
Generator current	3	60 *s*	A	Every 1 min	10.24 *kHz*
Wind speed	1	60 *s*	m/s	Every 1 min	50 *Hz*
Ultrasonic reflections	2	1 *s* with sensor excited at 80 *kHz*	Arbitrary amplitude	Every 20 min	100 *MHz*

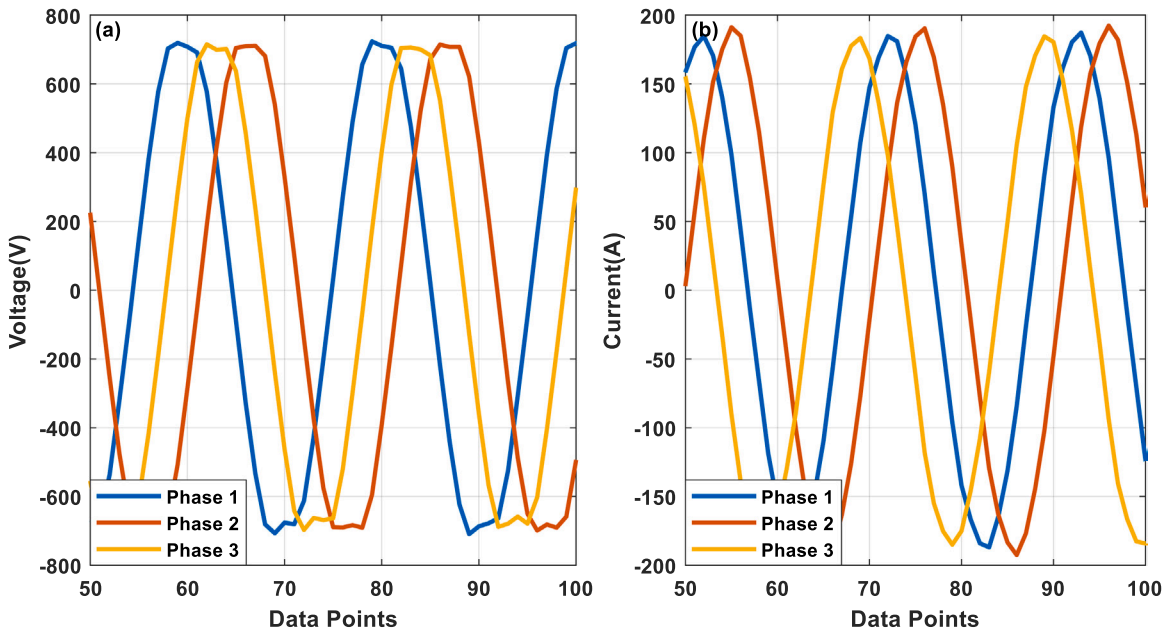

Fig. 5. (a) Voltage and (b) current measurements for all 3 phases.

current measurements were initially converted into root mean squared (r.m.s.) values before applying Eq. (1) where I_p and V_p are the r.m.s. current and voltage values for the phase whilst $\cos\varphi$ is the power factor of the generator, a constant at 0.89. The total power, P_{total} can subsequently be computed through summing the power of all the three phases as shown in Eq. (2).

$$P_{phase} = I_p V_p \cos\varphi \tag{1}$$

$$P_{total} = \sum_{i=1}^{3} P_{phasei} = \left(V_p I_p \cos\varnothing\right)_{phase1} + \left(V_p I_p \cos\varnothing\right)_{phase2} + \left(V_p I_p \cos\varnothing\right)_{phase3} \tag{2}$$

Wind speed measurements were directly obtained from the anemometer at a resolution of 0.1 *m/s* and required no pre-processing. A single average value was subsequently generated for both generator total power and wind speed for each captured dataset.

3.2. Ultrasound

Fig. 6(a) shows two raw signals captured at differing conditions by an ultrasonic transducer bonded onto a raceway surface. The blue waveform was captured when a roller was not directly incident on the sensor. The red waveform is a capture from when the roller was directly over the sensor location. Three pulses can be observed in Fig. 6(a), with their amplitudes decreasing from left to right. The first pulse was attributed to electrical excitation supplied to the sensor for generation of ultrasonic waves and thus is of no significance. Subsequent pulses were a result of reverberations from the roller-raceway interface. To maximize signal-to-noise ratio, a capture window was assigned to the first reflection, and this portion was extracted for further processing as illustrated in Fig. 6(b). Two bearing operating parameters were subsequently inferred from the data in the capture window containing first reflections, namely **roller load** and **bearing rotational speed**.

3.2.1. Roller load

Inferring roller load from ultrasonic measurements are well detailed in [42,43,49] and thus will only be summarised here. This is a two-step process where raceway deflection was initially inferred from ultrasonic measurements and subsequently a contact model was used to convert raceway deflection into roller load.

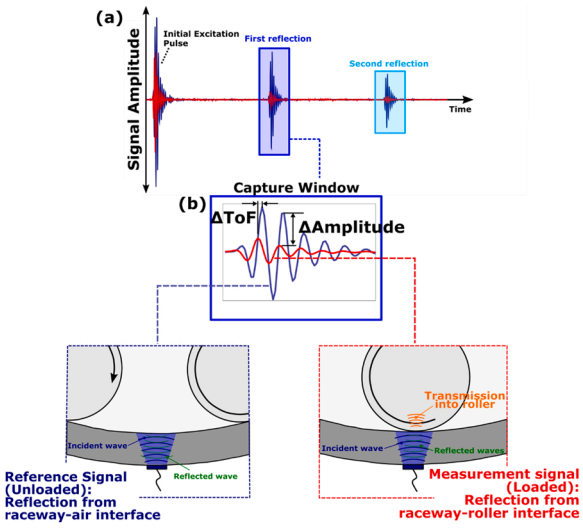

Fig. 6. (a) Raw ultrasonic signal showing initial excitation pulse alongside first and second reflections, and (b) first reflection from the roller-raceway interface showing difference in time-of-flight change (ΔToF) between the reference and measurement signal.

As mentioned previously, the blue signal was captured when no roller exists within the sensor's sensing region and thus the raceway is unloaded. This was taken as reference measurement. On the other hand, the red signal showed the effect of a loaded raceway on the measured signals. From Fig. 6(b), a time delay can be observed between the two pulses, where the loaded pulse led the reference pulse. This is primarily influenced by stress on the raceway exerted by the rollers. As the roller traverses into the sensor's sensing path, it deflects the raceway and changes the stress distribution of the raceway. The deflection reduces the ultrasonic waves' transmission path whilst the increase in compressive stress increases the rate at which the ultrasonic waves propagate (sound speed), resulting in a shorter Time-of-Flight (ToF). Apart from that, changes to the raceway surface (presence of lubricant and roller) will affect the phase of the ultrasonic wave, resulting in an apparent ToF change during processing. The contribution from this

apparent change was eliminated through data processing means, using a Hilbert Transform (see [42]). As such, the remaining contributions of time-of-flight change between the two pulses were raceway deflection, δ and variation in sound speed due to stress (acoustoelastic) [42]. This can be mathematically represented in Eq. (3) where L_{zz} is the acoustoelastic constant, experimentally quantified to be − 2.24 for bearing steel [42, 50] and $(c_{zz})_0$ is the unstressed speed of sound for bearing steel.

$$\Delta ToF = \frac{2(1 - L_{zz})\delta}{(c_{zz})_0} \tag{3}$$

Subsequently, Houpert's point contact model [51] shown in Eq. (4) was used for conversion of raceway deflection, δ into roller load, Q where R_x and $E^{'}$ are the reduced radius in x-direction and reduced modulus respectively ($R_x = 0.0131m^{-1}, E^{'} = 230.77GPa$), C_1 and C_2 are elliptical integrals ($C_1 = 1.7138$ and $C_2 = -0.2743$ are used for this study [51]), k is the ratio of reduced radius in y-direction to that of x-direction ($k = 758.4$). Point contact model was used instead of line contact as transitional values of deflection for line contacts were not exceeded at any point in this study, indicating that the bearing was lightly loaded.

$$Q = \frac{E^{'}\sqrt{R_x}}{{C_1}^{1.5}.k^{C_2 \cdot 1.5}} \cdot (2\delta)^{1.5} \tag{4}$$

Through combining Eqs. (3) and (4), a relationship between roller load, Q and ultrasonic time-of-flight change, ΔToF can be established:

$$Q = \frac{E^{'}\sqrt{R_x}}{{C_1}^{1.5}.k^{C_2 \cdot 1.5}} \cdot \left[\frac{\Delta ToF \bullet (c_{zz})_0}{(1 - L_{zz})}\right]^{1.5} \tag{5}$$

It is prudent to note that roller load, Q is the load transmitted through a single roller and not the bearing load. §4.3 details the necessary steps to convert roller load into bearing load, which considered the total sum of load transmitted through all the rollers. It should also be noted that conversion from deflection to load assumed a symmetrical, centrally aligned contact patch, i.e. that there was no misalignment of the contact. In cases where there is significant contact misalignment this conversion would not be valid. Finally, other sources of stress (such as hoop stress) may also affect results in extreme circumstances.

3.2.2. Bearing rotational speed

As well as load, ultrasound can be used to measure bearing speed, emitting the requirement for an additional sensor for this function. Fig. 6 (b) shows that in addition to the time shift, an amplitude difference between the reference and loaded measurements is also apparent. The reference measurements can be seen to possess a higher amplitude than the loaded signal (red). This amplitude variation is a result of the presence of roller within the sensing region. As the roller is directly located under the sensor, part of the ultrasonic energy is transmitted into the roller and causes a reduction in amplitude for the loaded measurements. This is further evident in the ultrasonic data stream shown in Fig. 7. This data stream consisted of ultrasonic pulses captured within the window, plotted alongside its respective acquisition time. The peak amplitudes of these pulses form the envelope for the data stream and dips within the envelope correspond to each roller pass. This was exploited to infer roller pass frequency, f_o and subsequently instantaneous bearing rotational speed, ω_{brg} as shown in Eq. (6) where Z is the number of rollers, d and D are the mean roller diameter and pitch diameter respectively and α is the outer race contact angle [43].

$$\omega_{brg} = \frac{120 \bullet f_o}{Z(1 - \frac{d}{D}\cos\alpha)} \tag{6}$$

3.3. Synchronisation and thresholding of measurements

Prior to using the generator power, wind speed and ultrasonically measured bearing speed as model inputs for the multi-body simulation, some pre-processing was necessary. Fig. 8 summarizes the full pre-processing procedure.

As the generator power and wind speed were sampled at different intervals compared to the ultrasonic measurements, synchronisation between the two acquisition systems was necessary as shown in Fig. 8 (step A). Since the ultrasonic measurements were taken at the least frequent interval (every 20 min), linear interpolation was carried out on the generator power and wind speed measurements instead. This was a necessary step for comparison of the data sets and due to the high sampling rate of CMS1, was unlikely to cause any issues with measurement distortion.

Fig. 8 shows the thresholding applied onto the wind speed and generator power measurements (step B). This was to ensure measurements considered in this study were taken during steady operation (within cut-in and cut-out wind speeds). Measurements captured below the generator's minimum operating power of 100 kW were also omitted.

Since the turbine in this study was a constant-speed wind turbine, under steady operating conditions the HSS will rotate at a constant speed of around 1550 RPM. As such, measurements outside of this region were also filtered out, as shown in Fig. 8 to eliminate data points

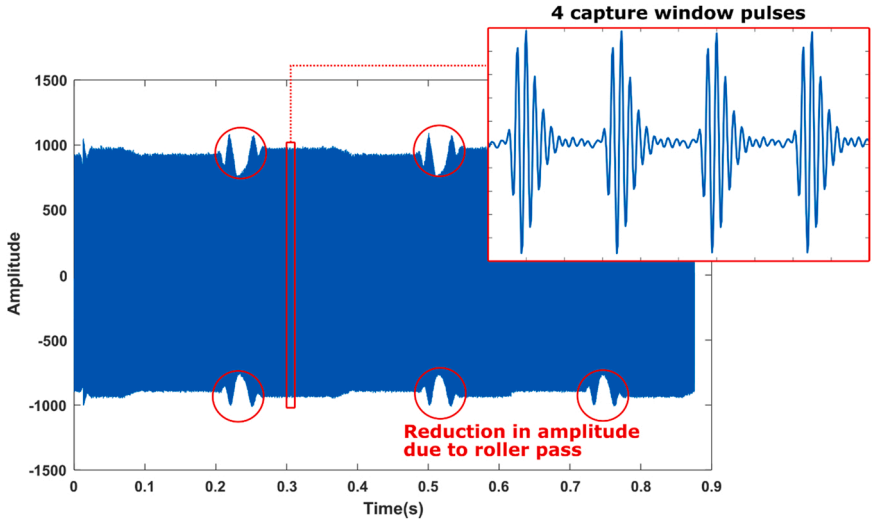

Fig. 7. Raw ultrasonic data stream consisting of capture window pulses. Reduction in amplitude observed within the data stream was a consequence of roller pass. The oscillations in amplitude on contact entry and exit are a result of sensor beam width being wider than the contact, and are discussed in more detail in [46,52].

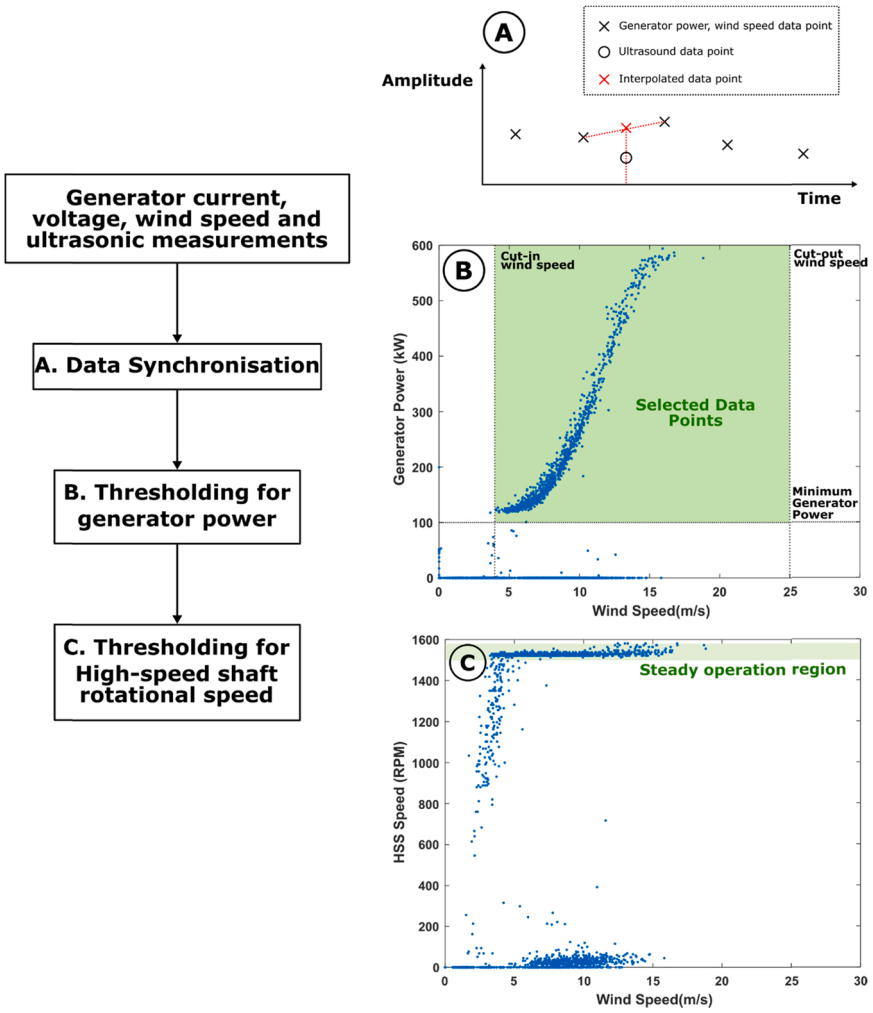

Fig. 8. Summary of pre-processing steps implemented on the generator power, wind speed and ultrasound measurements.

taken during start-up, shut down and idling (step C).

Fig. 9 shows the pre-processed ultrasonic inferred roller load measurements for both sensor channels against wind speed. As expected, an increase in wind speed resulted in an increase in roller load for both sensor channels at higher wind speeds, albeit with increasing scatter. Also, the roller load measurements for the sensor located at the centre of the maximum loaded region (CH2) is higher than CH1 as expected.

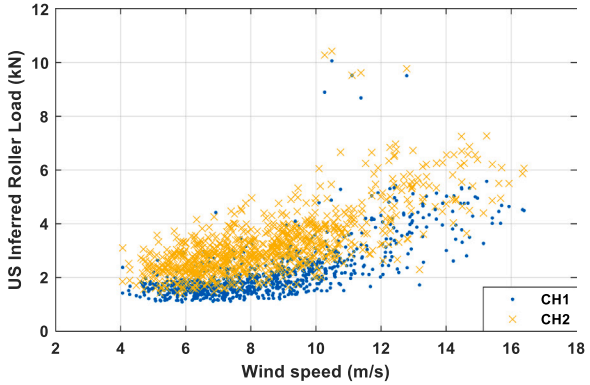

Fig. 9. Variation of ultrasonically inferred roller load with wind speed for sensors located at 241° (CH1) and 201° (CH2) clockwise from bearing TDC. after pre-processing.

4. Multibody modelling

4.1. SABR model of gearbox

A commercial multi-body model created using software, "SABR" developed by Ricardo PLC was used to validate the ultrasonic load measurements. SABR was used to simulate static loading of the full gearbox of the Vestas V42 wind turbine. The aim of the modelling was to simulate gearbox and subsequently bearing loading under stable operating conditions (4–25 *m/s* wind speed and 1550 *RPM* bearing rotational speed) and thus the model does not consider transient events such as wind gusts or grid power outage.

SABR consists of a shaft, gear and bearing conception and design package based on engineering standards (such as ISO 281:2007 [53] and ISO/TS 16281 [54]) as well as Ricardo's product design, manufacturing, and testing experience [55]. The software uses power flow to resolve the system. Ricardo optimised beam models were used to calculate shaft loads. The bearing load models used were based on relationships well summarised by Harris and Kotzalas [56].

Fig. 10 shows the geometrical assembly of the simulated gearbox component. The component was a Brook-Hansen EH 55 G21S-BN-50 gearbox, lubricated with VG320 gear oil. All the shaft, bearing and gear geometries and interfaces were recreated for all three stages of the gearbox with their material properties defined. Zero deflection boundary conditions were set using infinitely thin bearings where appropriate. The model requires either input or output shaft torque and shaft speed as boundary conditions.

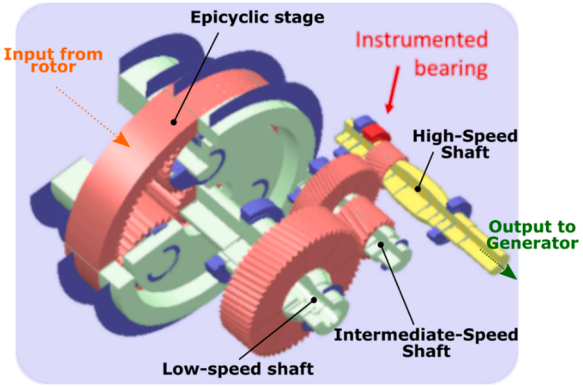

Fig. 10. Multibody model geometry.

4.2. Model input generation

Generator power, P_{total} and HSS speed, ω_{brg} measurements obtained from the field were used to define the boundary conditions for the model. To compute the HSS torque, τ_{HSS} the following relationship was used.

$$\tau_{HSS} = P_{total}/\omega_{brg} \tag{7}$$

As wind turbine generators have very high efficiencies [57], generator power losses were assumed to be negligible and since the bearing investigated was situated on the HSS, gearbox efficiency need not be accounted for.

Fig. 11 shows the HSS torque measurements plotted alongside wind speed, used as input data for the model. The data was initially grouped into sets across the range of wind speed values between integers of wind speeds (i.e., 4.5, 5.5, 6.5 *m/s*…). For each of the 13 bins, mean values were computed and error bars were established at ± 3 standard deviations from the mean, indicating 99% prediction intervals. These binned torque values were subsequently used to generate input torques for the model. As insufficient data points were available for wind speeds > 17 *m/s*, these data points were not considered. Since the turbine rated power was at 16 *m/s*, the torque values at wind speeds > 17 *m/s* would likely be similar to those observed within the 16–17 *m/s* bin, although variability in measurements may differ. With the addition of evaluating the range of torques at each wind speed, a total of 39 torque cases were evaluated by the model. The scatter can be seen to increase with wind speed up to approximately 12 *m/s*, after which it begins to decrease. This is likely a result of dominant scatter being in measured wind speed and the gradient being maximum at around 12 *m/s*. Scatter was therefore more prominent at these higher gradients.

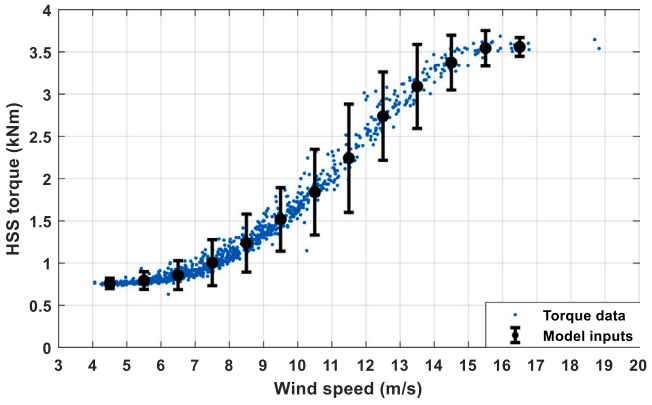

Fig. 11. HSS torque curve with model inputs. Central points of model inputs are mean values, and extremities of error bars show ± 3 standard deviations of binned values, taken at between wind speed integers (4.5, 5.5, 6.5 *m/s*…).

For the HSS speed measurements, no grouping of datasets was carried out but instead the mean operational value ± 3 standard deviations were directly computed across the full range of wind speeds. The value was found to be 1480 ± 5 *RPM*. Subsequently, the range of HSS torques shown in Fig. 11 along with the HSS speeds were combined as boundary conditions to input into the model. Each boundary condition case was then solved by resolving shaft loads until all loads were balanced to within 0.1 *mN*. The model was then used to output the radial and axial load acting on the instrumented HSS tapered roller bearing.

4.3. Prediction of Individual Roller Load

SABR predicted mean bearing load at the rated wind speed was 43.5 *kN*. This value was 10.8% and 71.3% of the bearing dynamic and fatigue load limit of 402 *kN* and 61 *kN* respectively. These percentages fell to 2.2% and 14.4% at the cut in wind speed of 4 *m/s*, showing that the bearing was lightly loaded relative to its load limits.

Since the multibody model outputs radial and axial bearing load, F_r and F_a, a conversion of maximum bearing load into roller load was necessary to facilitate comparison with the ultrasonic roller load measurements. This was done through using Eqs. (8) and (9) to calculate the bearing maximum circumferential load, $Q_{\max}$ and subsequently computing the roller load at 241° (CH1) and 201° (CH2) clockwise from the bearing top dead centre (TDC) (see Fig. 4), through using Eq. (10).

For a bearing under combined radial and axial load, the load on the single most heavily loaded element of the raceway, $Q_{\max}$ is given by Eqs. (8) and (9) respectively where F_r and F_a are the radial and axial load on the bearing, Z is the number of rolling elements at 20, and α is the outer race contact angle at 15.64°, $J_r(\epsilon)$ and $J_a(\epsilon)$ are the radial and axial load integrals respectively and ϵ is the load distribution factor [30].

$$Q_{\max} = \frac{F_r}{J_r(\epsilon)\cdot Z\cdot\cos\alpha} \tag{8}$$

$$Q_{\max} = \frac{F_a}{J_a(\epsilon)\cdot Z\cdot\cos\alpha} \tag{9}$$

The values for ϵ, $J_r(\epsilon)$, $J_a(\epsilon)$ were computed via their relationship with $F_r\tan\alpha/F_a$ [56]. The load at angle ψ from the centre of the maximum bearing loaded portion is given by Eq. (10), where n is the load-deflection exponent [56]. As mentioned in §3.2.1, since Houpert's transitional deflection from point to line contact was not exceeded in the roller load measurements, the contact was deemed to be point and as such an exponent, n of 1.5 was used.

$$Q_\psi = Q_{\max}\left[1 - \frac{1}{2\epsilon}(1-\cos\psi)\right]^n \tag{10}$$

Fig. 12 illustrates the SABR model simulated roller load for wind speeds between 4 and 17 *m/s* for two circumferential locations within the HSS bearing, corresponding to the centre of the maximum loaded region (CH2) and 40° from the centre of the maximum loaded region

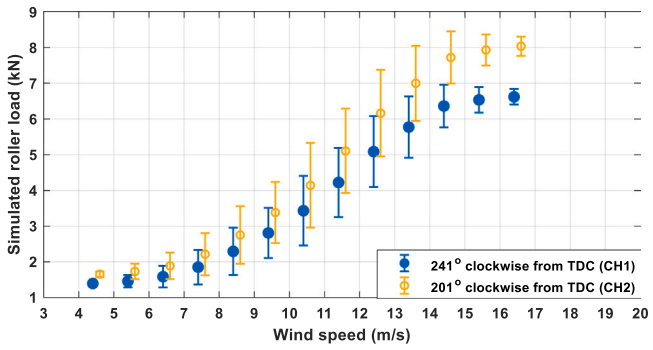

Fig. 12. Roller loads simulated using the multibody model for two bearing locations: at 241° (CH1) and 201° (CH2) clockwise from bearing TDC.

(CH1). The error bars correspond to the simulated load values obtained from the range of shaft torques and speeds used as boundary conditions and CH2 measurements were shifted slightly to the right to avoid superimposing the two datasets.

5. Results

5.1. Comparison of measured and modelled bearing load

Fig. 13 compares the ultrasonic load measurements obtained from the field to the simulated loading generated by the multibody model for the two bearing locations at 241° (CH1) and 201° (CH2) clockwise from bearing TDC. Both ultrasonic measurement channels show reasonable agreement with the multibody model predicted loads at 55.98% for CH1 and 48.54% for CH2. Both high and low value outliers exist for CH1 and CH2 with a significant portion of measurements falling under the latter category (31.38% and 37.47%). Conversely, high value outliers make up 12.64% and 13.99% of CH1 and CH2 measurements respectively.

Fig. 14 illustrates the percentage agreement for all wind speed clusters for both measured bearing locations (CH1, CH2). Both agreement plots resemble normal distribution with positive skewness with CH2 measurements showing better agreement between wind speeds of 8 – 11 *m/s* compared to CH1. For CH1 measurements, data captured between 6 and 9 *m/s* show the best agreement with increased error observed at higher wind speed values (>10 *m/s*). For the higher loaded bearing region (CH2), measurements show better agreement across the higher wind speed values from 8 to 11 *m/s*. The subsequent section explores the potential sources of errors which result in the discrepancies observed between the ultrasonically measured and multi-body modelled load values.

5.2. Load variability analysis

Potential contributing sources of error include variability in wind speed, error resulting from data synchronisation, and inherent error from the ultrasonic data acquisition hardware. These were investigated with the datasets available.

5.2.1. Variability in wind speed

When executing power curve fitting it is often assumed that the data represented by wind speed and power measurements can be regressed on to form the power curve [57,58]. In the current context we are interested in the fact that measuring wind speed is difficult due to the turbine seeing an effective (non-point) wind speed which can be thought of as a rotor average value. As such, there is significant 'noise' present when this wind speed is assumed to be a measurement of effective wind speed. For the purposes of power curve modelling this is less of an issue as the goal is normally to determine the link between measured wind speeds and output power for certification and production estimates. In these cases, regression is performed to identify an underlying relationship, with wind measurements tending to be interpreted as non-noisy input values and regression noise attributed to power values. Arguably, to properly capture the high noise values on measured wind speeds, regression should consider the noise on this input variable also. For the purposes of the current work the key question is then: *are the high noise levels on wind speed measurements the underlying cause of the scatter seen in* Fig. 13*?*. In order to investigate this question, it is proposed that a regression should be performed to smooth out the apparent noise on wind speed measurements so that Fig. 13 can be replotted with 'corrected' wind speed values to see whether this reduces observed scatter (with an affirmative answer indicating that wind speed noise is indeed a contributor).

The turbine operated at constant speed throughout its operation, with pitch control to maintain rated power once it was reached. Data points above a wind speed of 14 *m/s* were first eliminated from the dataset in order to ensure only data from the one operational region remained (the turbine rated wind speed was 16 *m/s*). For the remaining measurements (seen in Fig. 15) a regression was performed to smooth out noise on wind speed values. Note that it was assumed that the major noise contribution is on the wind speed variable (rather than power) and hence regression was performed with power treated as the input variable and wind speed as output variable, this is equivalent to a standard regression having swapped the x and y axes of Fig. 15(a). A Gaussian process (GP) regression [59] was performed since the underlying function is not expected to have a parametric form due to the fact that, although power in the wind increases cubically with wind speed, factors such as aerodynamic efficiency cause deviation from this simple form [57,58]. GP regression offers a non-parametric and flexible regression technique which fits a smooth curve to the data having optimised the fitting parameters using the data itself. Other nonparametric fitting techniques would be equally valid here, the aim being to smooth out wind speed measurement noise, and so there is nothing unique about the particular choice of fitting algorithm with respect to this problem. The outputs of this regression can also be seen in Fig. 15 (a). The fitted curve was then used to adjust measured wind speed values by taking the fitted wind speed corresponding to measured power at each measurement

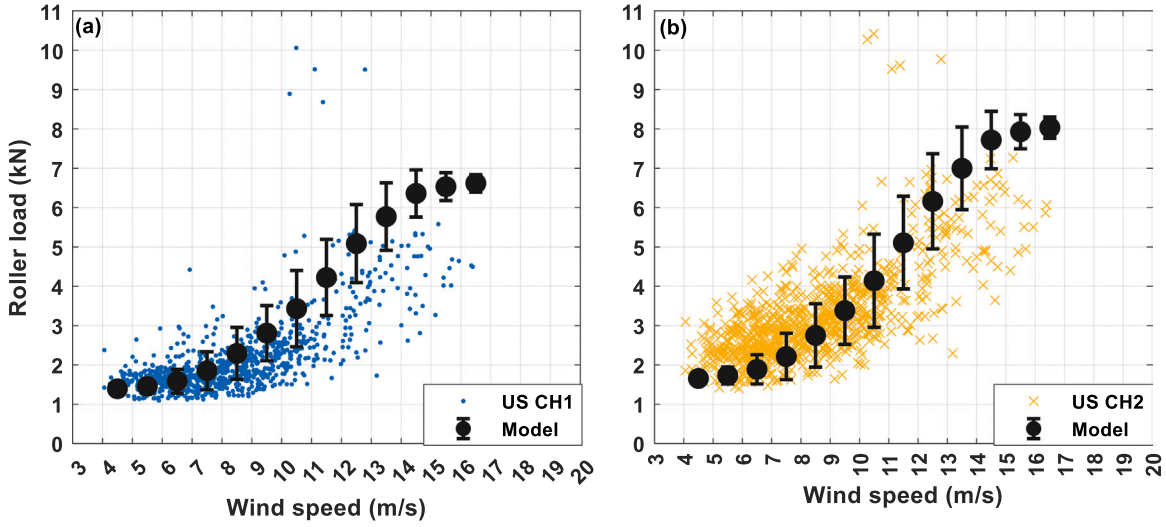

Fig. 13. Comparison between ultrasonically measured roller load and multibody model load values for two bearing locations at (a) 241° (CH1) and (b) 201° (CH2) clockwise from bearing TDC.

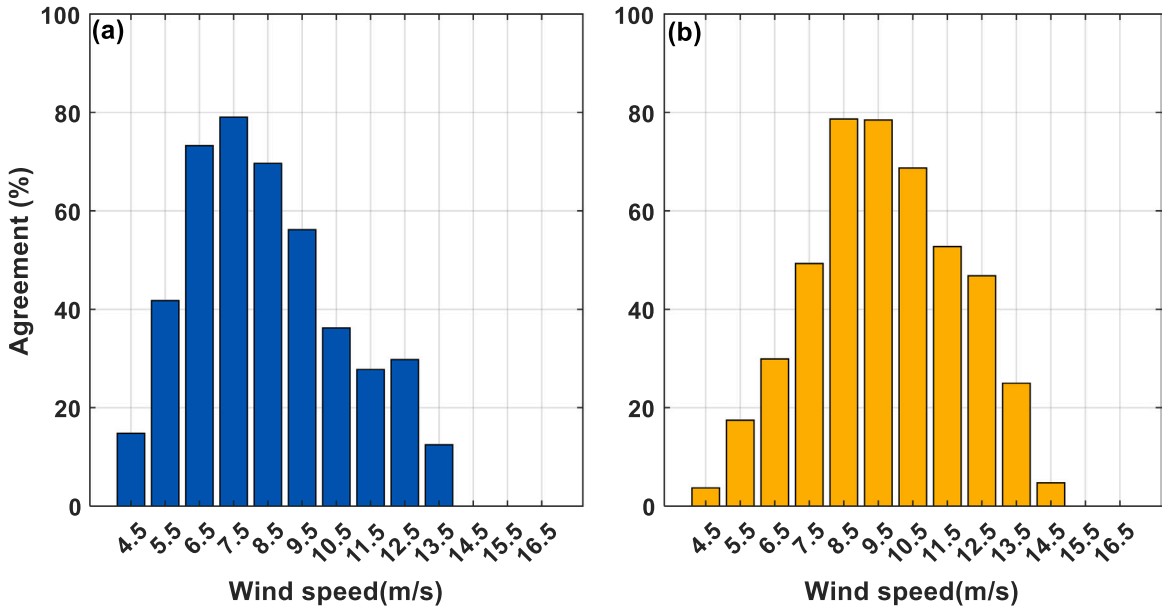

Fig. 14. Percentage agreement between modelled and US measured roller load for two bearing locations at (a) 241° (CH1) and (b) 201° (CH2) clockwise from bearing TDC.

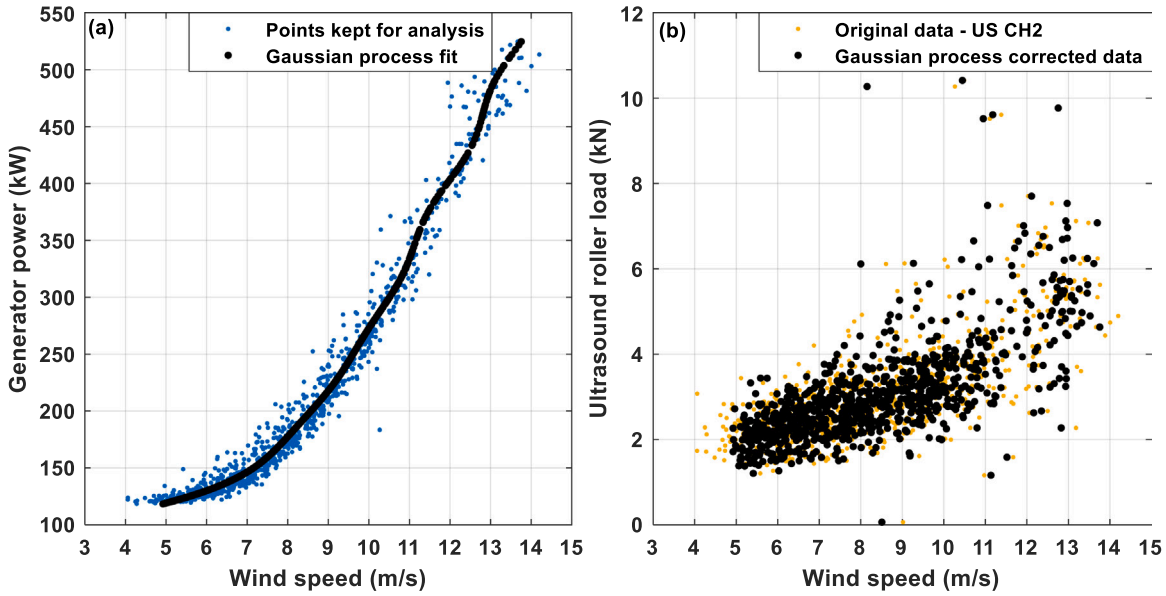

Fig. 15. (a) GP regression on the wind speed-generator power relationship, (b) Ultrasonic roller load measurement (CH2) before and after GP regression.

point.

Fig. 15 (b) shows the ultrasonic load measurements (CH2) with the GP corrected wind speed values. No real reduction in scatter due to the correction was observed, which suggested that wind speed measurement noise was not a significant contributing factor to the scatter of the ultrasonic load measurements, which was a surprising result.

At this stage it is prudent to state that other factors in the wind field may be the cause of variability in the ultrasound results. Variability in the wind field from features such as wind shear or turbulence may still cause variations in out of plane loading. This seems less likely to have caused variation due to the fact that the instrumented bearing is positioned reasonably far from the rotor, but this is possible, nonetheless. To investigate such phenomena, further knowledge of the wind field would be necessary, for which data was not available.

5.2.2. *Variability from non-synchronous datasets*

Since the generator power and wind speed are acquired at a different sampling interval compared to the ultrasonic measurements, potential error could originate from this due to interpolating of the measurements to synchronise all the measurements. The maximum time delay between the two data acquisition systems was found to be 20 s. If this was the case, data where there exists a long acquisition time delay between the ultrasound and wind speed measurements would show significant scatter compared to data points obtained under shorter acquisition time delay. Fig. 16 shows the variation in ultrasonic load measurement for CH2 with increasing wind speed where the acquisition delay between the ultrasound and wind speed/generator power measurements are at 2, 4, 7 and 20 s apart. Measurements seem to not exhibit an increase in scatter with increasing acquisition delay time. Interestingly, the highest extent of data scatter was observed in Fig. 16 (b), corresponding to an acquisition delay time of 4 *s*. Consequently, it is deemed unlikely for

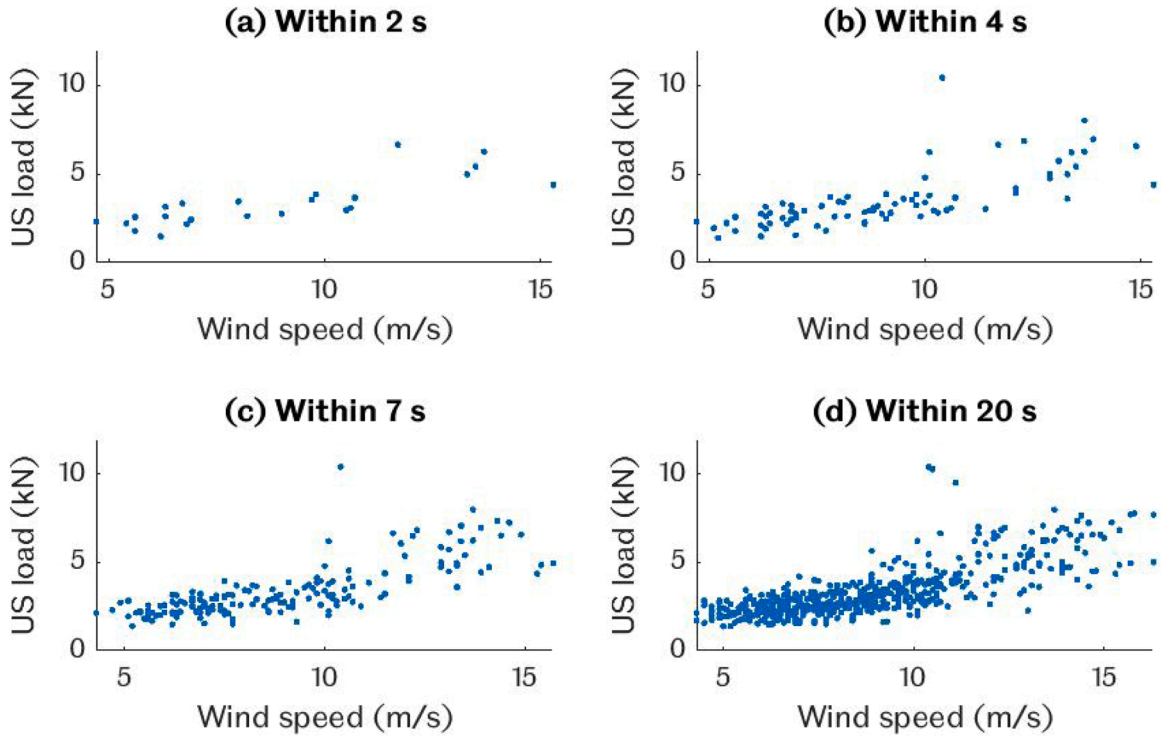

Fig. 16. Effect of non-synchronised measurements on ultrasound CH2 roller load scatter showing data points where wind speed data was captured within (a) 2 s, (b) 4 s, (c) 7 s and (d) 20 s of US data.

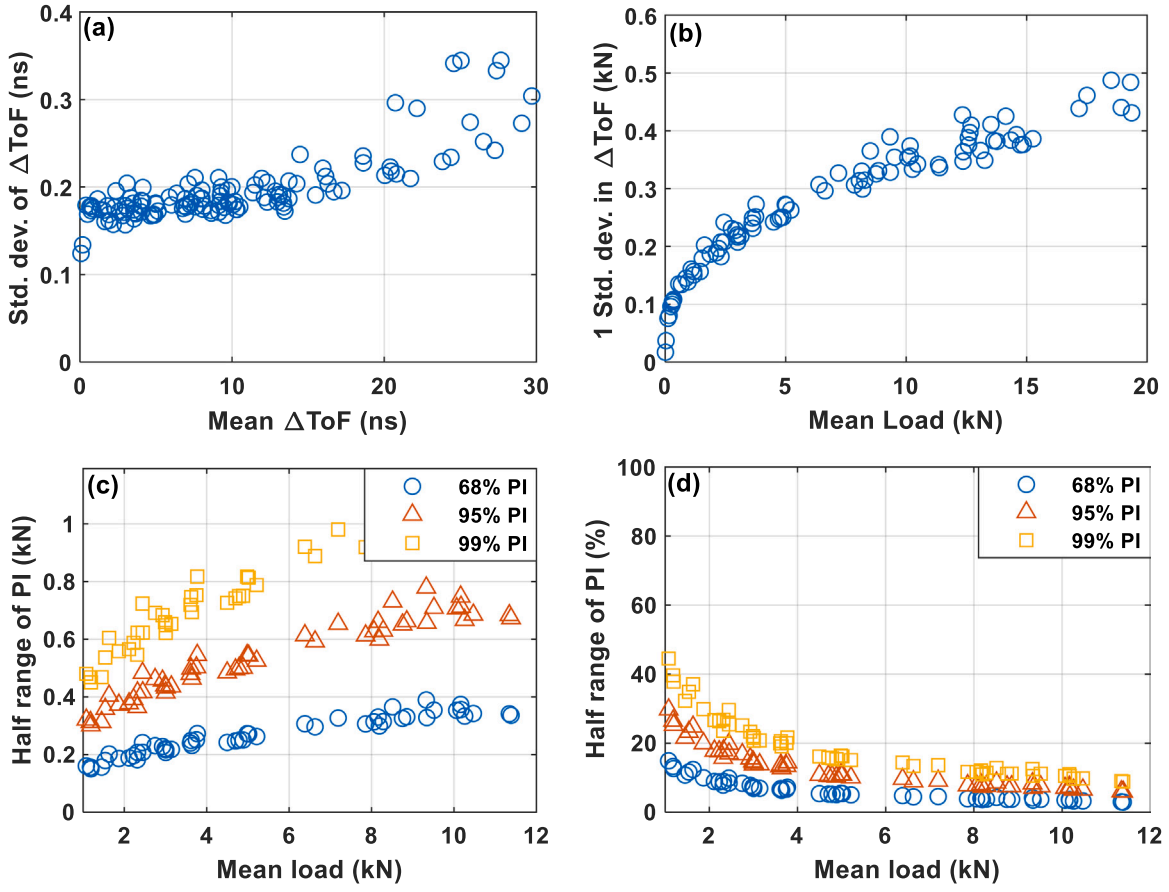

Fig. 17. (a) Comparison of mean and standard deviation of ΔToF, (b) ultrasound measurement error resulting from one standard deviation change in time of flight and load prediction intervals (PI) for loading range between 1 and 12 *kN* (c) in magnitude and (d) in percentage of mean.

non-synchronous data measurements to contribute to the discrepancy observed.

5.2.3. Variability from ultrasonic data acquisition hardware

As time-of-flight change of ultrasonic signals due to roller load are in the nanosecond scale and measurements were sampled in the same order (10 ns), it is highly likely that error would originate from the ultrasonic data sampling hardware and processing of the data. A higher sampling rate may reduce this error but would significantly increase the cost of acquisition hardware. To quantify the error, an experiment was conducted using the same model of data acquisition hardware which was employed for field measurements. The experiment conducted involved static compression of a cylindrical roller bearing raceway between 50 *kN* to 300 *kN* with 50 *kN* increments using a single roller with the aim of obtaining raceway deflections of a similar magnitude to those measured from the field instrumented HSS bearing. Ultrasonic measurements were subsequently taken at each load increment and converted to time-of-flight measurements through procedures detailed in §3.2. For each loading step, 250 pulses were captured, over a period of 2 s and each was compared with the modal signal resulting in 250 time shift measurements.

The variation in each of these data points incorporates several sources of error. These include error from signal noise, digitisation error, and error implicit in the data processing. For each of the data sets, the mean and standard deviation of the normally distributed measurement was computed, the results of which are shown in Fig. 17. The standard deviation of time-of-flight change, ΔToF showed a slight increase with mean value for ΔToF. This was potentially a result of a decrease in signal-to-noise ratio at higher load measurements (higher mean ΔToF). As more load is applied through a contact, deflection of the raceway increases but so does the stiffness of the contact. The increased stiffness resulted in higher signal transmission through the contact and subsequent reduction in the amplitude of the reflected signals while the noise level remains relatively constant.

Fig. 17 (b) shows the mean load and error from one standard deviation of ΔToF computed using ΔToF measurements shown in Fig. 17 (a). The absolute error values were seen to increase with increasing mean load. Fig. 17 (c) shows three prediction intervals (PI) generated through ± 1, ± 2 and ± 3 standard deviations from the mean load, corresponding to 68.3%, 95.5% and 99.7% confidence levels, for a loading range between 1 and 12 *kN* as observed from the field HSS measurements. Only the positive half of the prediction load was shown in the vertical axis. As the PI confidence level increases, more variation was observed within the measurements. Although the magnitude of error appears to increase with increasing load, the percentage of error relative to the mean load can be seen decreasing as shown in Fig. 17 (d). As such, measurements taken at a higher load would yield greater confidence in accuracy. Consequently, the ultrasonic load measurement technique can be said to be better suited for measuring bearings under higher loading (i.e. wind turbine main, pitch and gearbox cylindrical roller bearings). In this application there is a substantial amount of error in the ultrasonic load measurements.

The 99% PI data was subsequently incorporated into the error bars of Fig. 13 and the adjusted results and agreement bar chart were shown in Fig. 18 and Fig. 19 respectively. For measurements captured at 40° from the centre of the maximum loaded region (CH1, Fig. 18(a)), measurements between the modelled and measured loads achieved an 89.95% agreement with high and low value outlier datapoints still present, accounting for 2.71% and 7.34% of the measurements respectively. For CH2 measurements, the agreement was lower at 78.84% with 5 times more high value outlier datapoints (15.8%) and 30% less low value outlier datapoints (5.19%). Thus, it can be concluded that approximately one-third of the scatter (33.97% for CH1, 30.3% for CH2) were due to inherent hardware acquisition error.

Fig. 19 shows the percentage agreement between modelled and US measured roller load for CH1 and CH2 after incorporating error from ultrasonic data acquisition across various wind speeds. Measurements can be seen to agree better for both CH1 and CH2 with nearly 80% or greater agreement for measurements less than 11 *m/s* for CH1 and 13 *m/s* for CH2.

5.2.4. Modelling limitations and error

The previous sections were dedicated to identifying sources of errors originating from measured parameters (wind speed, ultrasound), however it is also prudent to consider limitations of the multi-body model. The model can only account for static loading of gearbox and thus will not include dynamic effects such as grid losses or wind gusts in the results.

Apart from that, the model assumes a certain load distribution within the bearing which may not be completely accurate as the pre-loading state of the bearing was unknown. We can verify this with the ultrasonic measurements, however. We can input the ratio between the ultrasonically measured loads to Eq. (10) to calculate a value of ϵ which

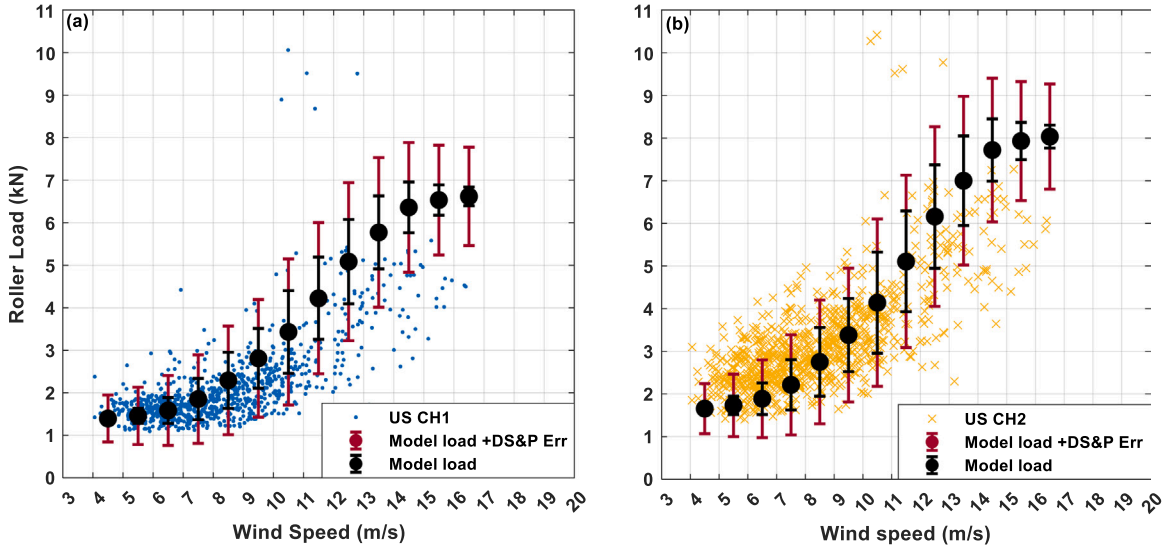

Fig. 18. Load comparison between ultrasound and model predicted loads for two bearing locations at (a) 241° (CH1) and (b) 201° (CH2) clockwise from bearing TDC. Error bars correspond to the range of input torques shown in Fig. 12 in addition to the error from ultrasonic data acquisition from Fig. 17(c).

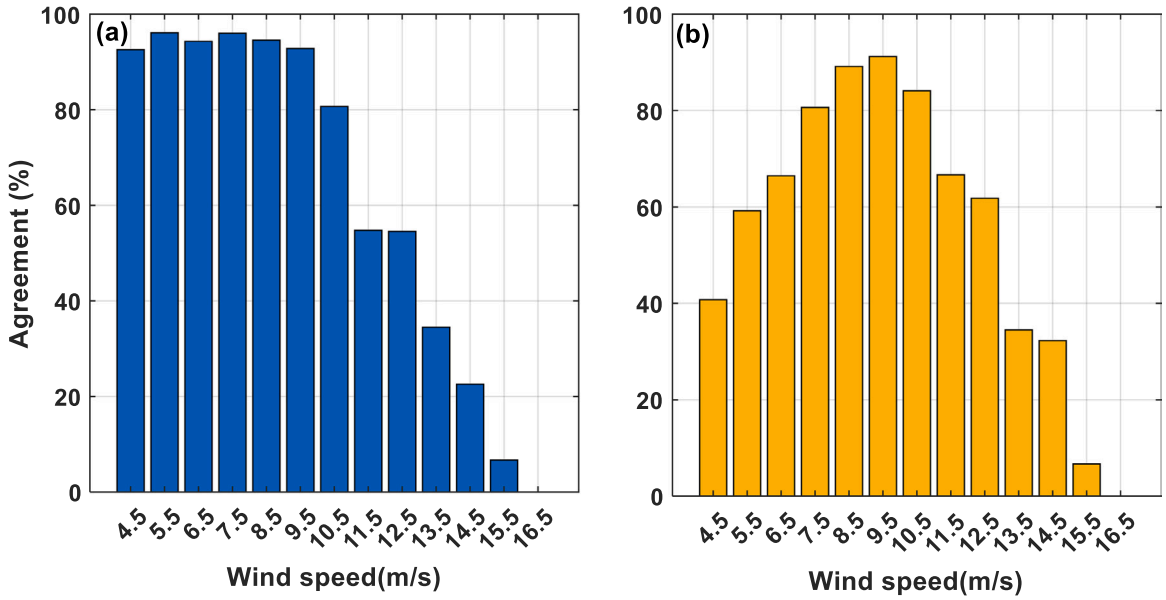

Fig. 19. Percentage agreement between modelled and US measured roller load for two bearing locations at (a) 241° (CH1) and (b) 201° (CH2) clockwise from bearing TDC after incorporating error from ultrasonic data acquisition.

describes the distribution of load around the bearing. The ratio had a mean value of 0.69 with measured values between 0.3 and 1 which is shown Fig. 20(b). This equates to an ϵ value of around 0.5 (range of 0.2 to inf) and shows that the actual load distribution in the bearing changed during operation and that the model was likely insufficient in this respect. The model value for ϵ was set at around 1. This would require a load ratio of around 0.82.

Finally, during the modelling process, the generator power was used to back calculate shaft torque. This may have had the effect of masking fluctuations in torque that would have explained the variability observed in the ultrasonic load measurements, as well as the high load outliers. There are other possible causes of discrepancies between the results such as varying levels of misalignment or raceway distortion.

6. Discussion

6.1. Dynamic behaviour of bearing with operation

High and low value outliers would still be present even if the modelled values observed in Fig. 18 were shifted upwards or downwards to account for the error in load distribution factor. One possible justification for the low and high load outliers would be that the bearing loaded zone may be shifting due to transient events such as grid losses or wind gusts. This would result in a c 241° (CH1) and 201° (CH2) from the bearing TDC. Such phenomenon was observed in the dynamometer testing conducted by NREL [36], where the maximum loaded zone shifted completely as a result of an induced braking event.

Fig. 20(a) shows the roller load measurements for two bearing

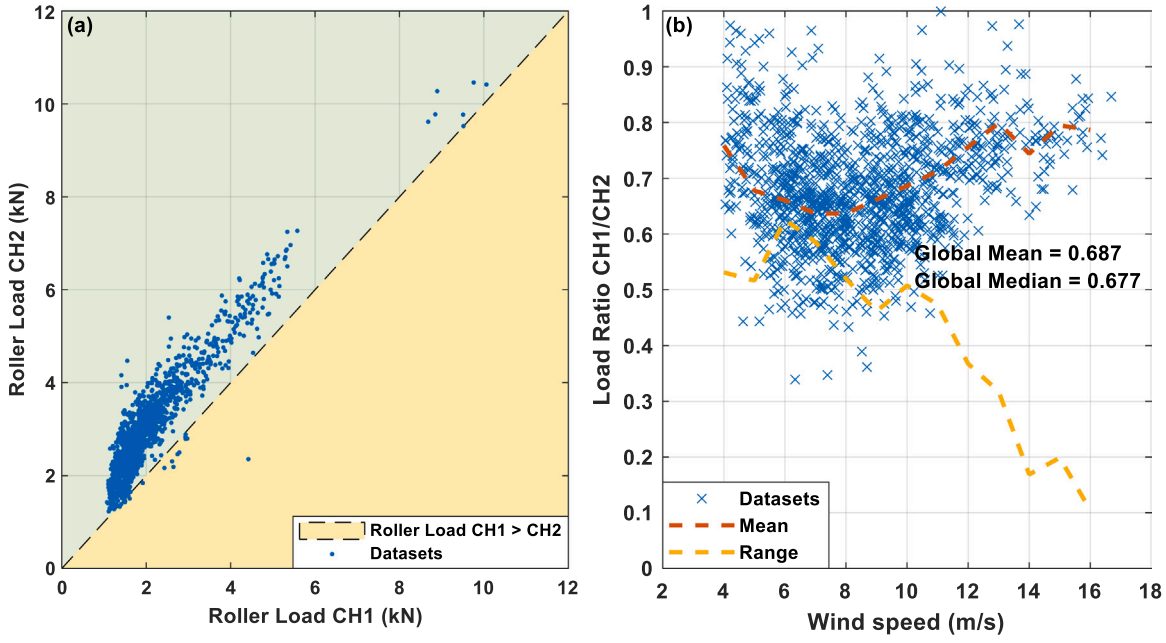

Fig. 20. (a) Roller load measurements obtained at the edge (CH1) against measurements obtained at the centre (CH2) of the maximum loaded region, (b) Load ratio between CH1 and CH2.

locations at 241° (CH1) and 201° (CH2) from the bearing TDC. If measurements fall within the lower yellow quartile, roller load measurements from CH1 would be greater than CH2 which would indicate a complete shift in loading zone and conversely, no complete loading zone shift occurs if it falls within the upper quartile (green). Most of the datasets fall within the latter condition apart from a small percentage (~1%) which exceeded this, indicating some transient event. Fig. 20(b) shows the gradient or ratio of the two load measurements, $(Q_{\varphi}/Q_{\max})$ obtained at the centre (CH2) and 40° from the centre of the maximum loaded region (CH1). Mean (amber) and range (yellow) values of the ratio were also included in the plot. Considerable scatter can be seen as the values fluctuate with a range of 0.53 at 4 *m/s* which decreases with higher wind speed. This indicates that as the bearing loading increases with wind speed, the tolerance within the system is gradually consumed which subsequently consolidates the bearing loading region. On the other hand, for the mean load ratio, loading at 241° from the TDC (CH1) can be seen to initially decrease from between 4 and 8 *m/s* but gradually increase at wind speeds greater than 8 *m/s* up to 0.79 of CH2, indicating a slight shift in bearing loaded zone during turbine operation. The global mean value for the measured load ratio was found to be 0.687 which agreed well with the theoretical ratio of 0.67 [22].

It was established through laboratory testing in §5.2.3, the variation (standard deviation) of roller load purely resulting from data acquisition sampling error. Consequently, any variation greater than this would be a result of bearing operation. Fig. 21 shows the variation in roller load in each one second capture with mean roller load with a yellow-coloured portion of the plot showing variation due to inherent measurement error computed from §5.2.3. Each marker shown within the figure corresponds to a dataset and measurements shown were for when the HSS is rotating at maximum speed of 1550 *RPM*. Since all the data points fell within the green zone, it can be said that part of the variation in roller load is due to bearing operation. This might be due to roller dimensional variation or rotational concentricity of bearing components. For CH1 measurements, the percentage variation in roller load were seen to decrease from 20% at around 2*kN* down to just less than 10% at around 5*kN*. Majority of the data points were concentrated between 2 and 6*kN* with some captured between 8 and 10*kN*. A similar trend of decreasing variation was also observed in Fig. 21(b). The reduction in variation of roller load as load increases could potentially be due to the reduced clearance for bearing and drivetrain components as tolerances within the system are consumed with increasing load.

6.2. Consequences of low and high outlier loading

For the outlier measurements, both high and low values were present within the ultrasonic measurements, comprising more of the latter. Both are a cause for concern. Low loads can be damaging as bearings may lose traction and skid [60,61]. Skidding increases the risk of raceway damage from smearing and as a consequence could lead to a reduction in fatigue life and accelerate bearing failure [61]. Apart from that, skidding is also theorised to be a factor that promotes WEC formation and propagation [12,62] which subsequently leads to premature bearing failure through axial cracking.

For overloading, these outlier loads can be up to 293% (CH1) or 252% (CH2) higher than the predicted mean loading under steady operating conditions. A 293% increase in bearing load will result in more than 35-fold reduction in L_{10} bearing life whilst a 252% increase will cause a 22-fold decrease in life. These high load outliers however only account for 0.56% (5 data points) of the dataset for both measurement locations but would still lead to some reduction in L_{10} bearing life. It is also prudent to note that since only one second of ultrasonic measurements were taken every 20 min, translating to 3 s of measurement per hour, the ultrasonic measurement coverage was less than 0.1%. With increased measurement coverage it would be sensible to assume that further outlier datapoints, both low and high, would be observed, and their frequency of occurrence could be determined. The frequency of occurrence may be higher or lower than the ~0.1% coverage observed by the current dataset.

Apart from a reduction in bearing L_{10} life, high bearing load could cause overloading [9] and influence the bearing stress history [14] both of which are stipulated to promote premature bearing failure through WECs. As the HSS bearing experiences instances of high loading, it would be sensible to assume that the full gearbox experiences such events, and the loading would increase proportionately across the intermediate and low speed gearbox stages. Such events would result in reduction of bearing life as well as encourage subsurface crack formation and propagation at non-metallic inclusions or crack within the bearing [9,10,14], which gradually propagate to bearing surface and cause premature bearing failure. High loading across the gearbox stages would also increase the risk of pitting and spalling of gear teeth [21,63].

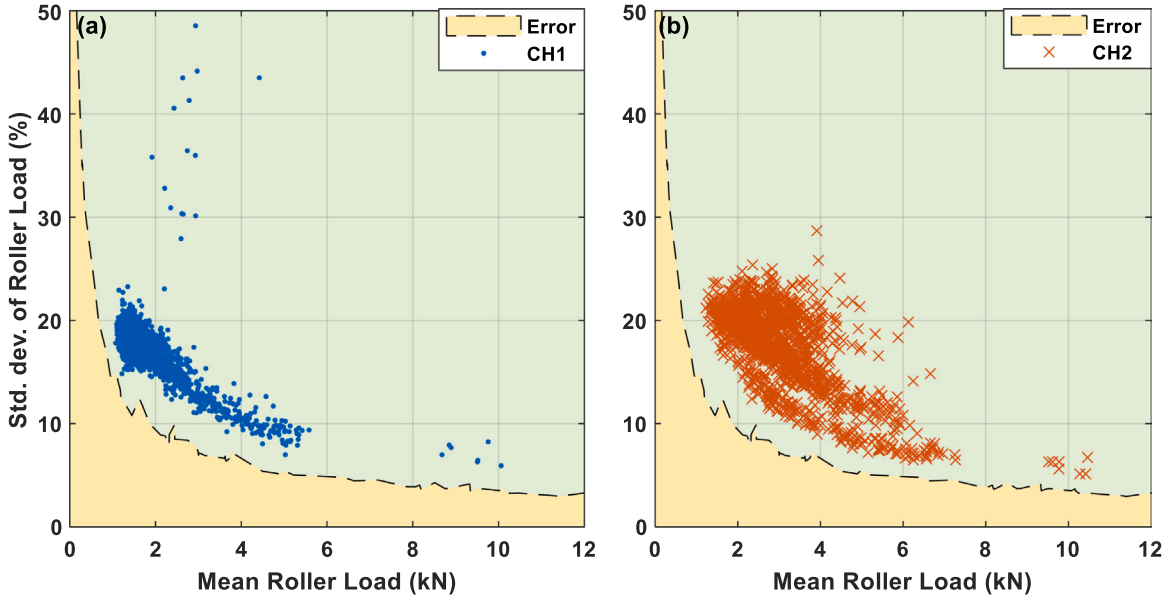

Fig. 21. Percentage variation in roller load (standard deviation) measured from sensor positioned at both the (a) edge and (b) centre of the HSS bearing maximum loaded zone.

Effects of high and variable bearing load is also apparent in main bearings where low rotational speed limits lubricant entrainment and high stresses result in poor lubricant separation between the rolling surfaces. This causes micro-pitting which alters the roller-raceway contact geometry. The micro-spalls on the surface acts as stress raisers which subsequently accelerates bearing failure through classical sub-surface initiated rolling contact fatigue [5,22,64]. There has been limited studies conducted on the statistics (frequency, failure mode) of main bearing failures. However, it is apparent that this is a problem as the industry is gradually shifting away from rolling element bearings and towards hydrodynamically lubricated main bearing designs [65–67].

6.3. Developments for further insights

This first implementation of ultrasonic measurement of wind turbine bearings gives some important lessons learned in addition to those detailed in [43]:

- The importance of coupling ultrasonic data with other measurements has been highlighted by the inability to infer the cause of transient events from the current data set. A better understanding of the wind field acting on the turbine and its transient nature, as well as accurate monitoring of events such as grid disconnections would be invaluable in ultrasonic data analysis.
- Additional sensors on the bearing would allow a more complete insight into bearing load during operation. More circumferential sensors would give a more complete picture of load zone movement and sensors along the axis of the bearing would enable analysis of axial load distribution and misalignment during operation.
- The ultrasonic load monitoring technique is more suited to higher load bearings such as main, planetary gearbox or pitch bearings.
- Attempts to reduce the error in ultrasonic load measurements should be made. A possible area for improvement is increasing A-scan acquisition frequency.

7. Conclusions

Field ultrasonic load measurements obtained from an instrumented HSS gearbox bearing from a Vestas V42 600 kW wind turbine located in Donegal, Ireland were compared with multi-body simulated load values. Generator power and HSS speed were used as inputs for the multibody model. Ultrasonic roller load measurements agreed well with the modelled results under turbine steady operating conditions, with up to 90% agreement.

The inherent error in ultrasonic load measurements has been statistically analysed and put into the context of wind turbine bearing load for the first time.

- Measurement accuracy was load dependent and ranged from ± 0.4–1.0 kN for a loading range of 0 – 12 kN (99% PI).
- Error analysis of the ultrasonic load measurements suggested that for higher accuracy, the method is better suited for bearings under high load (i.e. pitch, main or planetary bearings).

Despite significant error in ultrasonic measurements, the data still provided valuable insights into bearing operation:

- Low and high load outliers were identified, with the former accounting for a higher portion of the measurements. These were attributed to transient loading events, enabled by the static multi-body model of the drivetrain which did not capture these events.
- A slight shift in bearing loaded zone was observed throughout the bearing operation.
- Variation in load between rollers in a compliment was observed, as was variation in load ratio between the two circumferential locations. Both of these variations reduced at higher operating wind speeds, likely as the clearance of the drivetrain was consumed with increased loading

CRediT authorship contribution statement

B.P. Clarke: Methodology, Formal analysis, Investigation, Writing – original draft, Writing – review & editing, Visualization. **G. Nicholas:** Formal analysis, Investigation, Data curation, Writing – original draft, Writing – review & editing, Visualization. **E. Hart:** Formal analysis, Writing – original draft, Writing – review & editing. **H. Long:** Writing – review & editing. **R.S. Dwyer-Joyce:** Resources, Writing – original draft, Writing – review & editing, Supervision, Project administration, Funding acquisition.

Declaration of Competing Interest

The authors declare the following financial interests/personal relationships which may be considered as potential competing interests: R. S. Dwyer-Joyce has patent #15744289.8–1554 licensed to Ricardo plc. Ricardo plc provided, at no cost, a 1 year SABR academic license and an existing gearbox model to B.P. Clarke for use in this research.

Data Availability

Data will be made available on request.

Acknowledgments

The authors would like to acknowledge the financial support of the Engineering and Physical Sciences Research Council for part funding this research through RDJ's fellowship on *Tribo-Acoustic Sensors* EP/N016483/1 and the *Centre for Doctoral Training in Integrated Tribology* EP/L01629X/1. This work was also part conducted under the OWDin (Offshore Wind Drivetrain Innovation) led by Ricardo UK Ltd and funded by the Department of Energy and Climate Change, DECC. E. Hart is funded by a Brunel Fellowship from the Royal Commission for the Exhibition of 1851. The authors would also like to thank Tom Howard of the University of Sheffield and David Ferguson of the University of Strathclyde, Michael Wheeldon, and Jon Wheals of Ricardo plc for their contribution to the project.

Statement of Originality

This is to certify that to the best of my knowledge, the content of this paper is the authors own work. This paper has not been submitted for publication previously, is not under consideration elsewhere, has the full consent of all authors, and that, if accepted, will not be published elsewhere in the same form, in English or in any other language, without the written consent of the Publisher.

Benjamin P Clarke.

References

[1] Reder MD, Gonzalez E, Melero JJ. Wind turbine failures - tackling current problems in failure data analysis. J Phys 2016;753:072027.
[2] Carroll J, McDonald A, McMillan D. Failure rate, repair time and unscheduled O&M cost analysis of offshore wind turbines: reliability and maintenance of offshore wind turbines. Wind Energy 2016;19(6):1107–19.
[3] Sheng, S., 2013, *Report on Wind Turbine Subsystem Reliability - A Survey of Various Databases*, NREL.
[4] J. Keller, S. Sheng, J. Cotrell, A. Greco, Wind Turbine Drivetrain Reliability Collaborative Workshop: A Recap NREL/TP–5000-66593, DOE/GO 102016–4878 2016 1314863.
[5] Hart, E. , Clarke, B. , Nicholas, G. , Amiri, A.K. , Stirling, J. , Carroll, J., et al. , 2020, "A Review of Wind Turbine Main Bearings: Design, Operation, Modelling, Damage Mechanisms and Fault Detection," p. 20.
[6] Schwack F, Halmos F, Stammler M, Poll G, Glavatskih S. Wear in wind turbine pitch bearings—a comparative design study. Wind Energy 2022;25(4):700–18.

[7] Shuangwen, S., 2014, *Gearbox Reliability Database: Yesterday, Today, and Tomorrow*, NREL.
[8] Williams, L., Desai, A., Guo, Y., Sheng, S., and Phillips, C., 2021, *Machine Learning for Gearbox Fault Prediction by Using Both Scada and Modeled Data,* NREL.
[9] Evans M-H, Richardson AD, Wang L, Wood RJK. Serial sectioning investigation of butterfly and white etching crack (WEC) formation in wind turbine gearbox bearings. Wear 2013;302:1573–82.
[10] Evans M-H, Richardson AD, Wang L, Wood RJK, Anderson WB. Confirming subsurface initiation at non-metallic inclusions as one mechanism for white etching crack (WEC) formation. Tribol Int 2014;75:87–97.
[11] Vegter RH, Slycke JT. The Role of Hydrogen on Rolling Contact Fatigue Response of Rolling Element Bearings, 7. ASTM International; 2009.
[12] Ruellan A, Kleber X, Ville F, Cavoret J, Liatard B. Understanding white etching cracks in rolling element bearings: formation mechanisms and influent tribochemical drivers. Proc Inst Mech Eng, Part J: J Eng Tribology 2015;229(8):886–901.
[13] Gould B. Investigating the process of white etching crack initiation in bearing steel. Tribol Lett 2016:14.
[14] Manieri F, Stadler K, Morales-Espejel GE, Kadiric A. The origins of white etching cracks and their significance to rolling bearing failures. Int J Fatigue 2019;120:107–33.
[15] Bruce T, Rounding E, Long H, Dwyer-Joyce RS. Characterisation of white etching crack damage in wind turbine gearbox bearings. Wear 2015;338–339:164–77.
[16] Solano-Alvarez W, Bhadeshia HKDH. White-etching matter in bearing steel. Part II: distinguishing cause and effect in bearing steel failure. Metal Mater Trans A 2014;45A:4916–31.
[17] Bhadeshia, H.K.D.H., and Solano-Alvarez, W., "Critical Assessment 13: Elimination of White Etching Matter in Bearing Steels," Materials Science and Technology, 31 (9), pp. 1011–1015.
[18] Hiraoka K, Fujimatsu T, Tsunekage N, Yamamoto A. Generation process observation of micro-structural change in rolling contact fatigue by hydrogen-charged specimens. Jpn J Tribol 2007;52(12).
[19] Struggl S, Berbyuk V, Johansson H. Review on wind turbines with focus on drive train system dynamics: review on wind turbines. Wind Energy 2015;18(4):567–90.
[20] Nejad AR, Keller J, Guo Y, Sheng S, Polinder H, Watson S, et al. Wind turbine drivetrains: state-of-the-art technologies and future development trends. Wind Energy Sci 2022;7(1):387–411.
[21] Junior, V.L.J., Basoalto, H., Dong, H., Marquez, F.P.G., and Papaelias, M., 2018, "Evaluating the Challenges Associated with the Long-Term Reliable Operation of Industrial Wind Turbine Gearboxes," IOP Conference Series: Materials Science and Engineering, 454(012094).
[22] Kotzalas MN, Doll GL. Tribological advancements for reliable wind turbine performance. Philos Trans R Soc A: Math, Phys Eng Sci 2010;368:4829–50.
[23] Liu Z, Zhang L. A review of failure modes, condition monitoring and fault diagnosis methods for large-scale wind turbine bearings. Measurement 2020;149:107002.
[24] Doll GL. Surface engineering in wind turbine tribology. Surf Coat Technol 2022;442:128545.
[25] Dhanola A, Garg HC. Tribological challenges and advancements in wind turbine bearings: a review. Eng Fail Anal 2020;118:104885.
[26] Gould BJ, Burris DL. Effects of wind shear on wind turbine rotor loads and planetary bearing reliability: pitch moments as contributors to wind turbine bearing failure. Wind Energ 2016;19(6):1011–21.
[27] Hart E. Developing a systematic approach to the analysis of time-varying main bearing loads for wind turbines. Wind Energy 2020;23(12):2150–65.
[28] Guo, Y., and Keller, J., 2013, "Model Fidelity Study of Dynamic Transient Loads in a Wind Turbine Gearbox: Preprint."
[29] Hart E, Stock A, Elderfield G, Elliott R, Brasseur J, Keller J, et al. Impacts of wind field characteristics and non-steady deterministic wind events on time-varying main-bearing loads. Wing Energy Sci 2022;7(3):1209–26.
[30] Helsen J, Vanhollebeke F, Marrant B, Vandepitte D, Desmet W. Multibody modelling of varying complexity for modal behaviour analysis of wind turbine gearboxes. Renew Energy 2011;36:3098–113.
[31] Peeters JLM, Vandepitte D, Sas P. Analysis of internal drive train dynamics in a wind turbine. Wind Energy 2005;9:141–61.
[32] Hart E, Turnbull A, Feuchtwang J, McMillan D, Golysheva E, Elliott R. Wind energy - 2019 - hart - wind turbine main-bearing loading and wind field characteristics. Wind Energy 2019;22:1534–47.
[33] Yan Y. Load characteristic analysis and fatigue reliability prediction of wind turbine gear transmission system. Int J Fatigue 2020;130:105259.
[34] Li Z, Wen B, Peng Z, Dong X, Qu Y. Dynamic modeling and analysis of wind turbine drivetrain considering the effects of non-torque loads. Appl Math Model 2020;83:146–68.
[35] Wang S, Nejad AR, Moan T. On design, modelling, and analysis of a 10–MW medium-speed drivetrain for offshore wind turbines. Wind Energy 2020;23(4):1099–117.
[36] Park Y, Park H, Ma Z, You J, Shi W. Multibody dynamic analysis of a wind turbine drivetrain in consideration of the shaft bending effect and a variable gear mesh including eccentricity and nacelle movement. Front Energy Res 2021;8:604414.
[37] Guo Y, Keller J. Investigation of high-speed shaft bearing loads in wind turbine gearboxes through dynamometer testing. Wind Energy 2018;21(2):139–50.
[38] SKF, 2021, "Raising The Bar For Collecting Bearing Data," Evolution.
[39] Dwyer-Joyce, R.S., Drinkwater, B.W., and Donohoe, C.J., 2003, "The Measurement of Lubricant–Film Thickness Using Ultrasound," Proceedings of the Royal Society of London. A. Mathematical and Physical Sciences, 459, pp. 957–976.
[40] Zhang K, Meng Q, Zhao W. Measurement of oil film thickness in cylindrical roller bearing by ultrasound. Engineering Systems; Heat Transfer and Thermal Engineering; Materials and Tribology; Mechatronics; Robotics, Volume 3. Copenhagen, Denmark: American Society of Mechanical Engineers; 2014.
[41] Li M, Jing M, Chen Z, Liu H. An improved ultrasonic method for lubricant-film thickness measurement in cylindrical roller bearings under light radial load. Tribol Int 2014;78:35–40.
[42] Takeuchi A. Observation of lubrication conditions using an ultrasonic technique. Lubr Sci 2009;21:397–413.
[43] Chen, W., Mills, R., and Dwyer-Joyce, R.S., 2015, "Direct Load Monitoring of Rolling Bearing Contacts Using Ultrasonic Time of Flight," Proceedings of the Royal Society A: Mathematical, Physical and Engineering Sciences, 471 (20150103).
[44] Nicholas G, Howard T, Long H, Wheals J, Dwyer-Joyce RS. Measurement of roller load, load variation, and lubrication in a wind turbine gearbox high speed shaft bearing in the field. Tribol Int 2020;148:106322.
[45] Nicholas G, Clarke BP, Dwyer-Joyce RS. Detection of lubrication state in a field operational wind turbine gearbox bearing using ultrasonic reflectometry. Lubricants 2021;9(1):6.
[46] Ricardo Innovations, "OWDIn" [Online]. Available: https://innovations.ricardo.com/projects/owdin-en. [Accessed: 08-Sep-2022].
[47] Howard, T.P., 2016, "Development of a Novel Bearing Concept for Improved Wind Turbine Gearbox Reliability," PhD, The University of Sheffield.
[48] Ferguson, D., 2015, *Installation of Wind Turbine Condition Monitoring Equipment at Barnesmore Wind Farm*, University of Strathclyde.
[49] Ricardo, 2014, "Ricardo Showcases 'Life' Innovations for Reduced Cost of Wind Energy" [Online]. Available: https://ricardo.com/news-and-media/news-and-press/ricardo-showcases-%E2%80%98life%E2%80%99-innovations-for-reduced-c. [Accessed: 08-Sep-2022].
[50] Mills, R., Dwyer-Joyce, R., Hunter, A., and Chen, W., 2016, "Deriving Contact Stress or Contact Load Using Ultrasound Data."
[51] Nicholas, G., 2021, "Development of Novel Ultrasonic Monitoring Techniques for Improving the Reliability of Wind Turbine Gearboxes," The University of Sheffield.
[52] Houpert L. An engineering approach to hertzian contact elasticity—Part I. J Tribol 2001;123(3):582–8.
[53] Clarke, B.P., 2022, "Development of Ultrasonic Techniques for Rolling Element Bearing Monitoring," PhD, University of Sheffield.
[54] International Organisation for Standardisation, 2007, *ISO 281:2007. Rolling Bearings – Dynamic Load Ratings and Rating Life.*
[55] International Organisation for Standardisation, 2008, ISO/TS 16281:2008. Rolling Bearings – Methods for Calculating the Modified Reference Rating Life for Universally Loaded Bearings.
[56] Ricardo, "SABR" [Online]. Available: https://software.ricardo.com/products/sabr.
[57] Harris T, Kotzalas M. Rolling Bearing Analysis: Essential Concepts of Bearing Technology. CRC Press; 2007.
[58] Sohoni V, Gupta SC, Nema RK. A critical review on wind turbine power curve modelling techniques and their applications in wind based energy systems. J Energy 2016;2016:8519785.
[59] Carrillo C, Montano AFO, Cidras J, Dıaz-Dorado E. Review of power curve modelling for wind turbines. Renew Sustain Energy Rev 2013;21:572–81.
[60] Rasmussen CE, Williams CKI. Gaussian Processes for Machine Learning. The MIT Press; 2005.
[61] Jain, S., and Hunt, H., 2011, "A Dynamic Model to Predict the Occurrence of Skidding in Wind-Turbine Bearings," Journal of Physics: Conference Series, 305 (012027).
[62] Garabedian, N.T., Gould, B.J., Doll, G.L., and Burris, D.L., "The Cause of Premature Wind Turbine Bearing Failures: Overloading or Underloading?," TRIBOLOGY TRANSACTIONS, p. 11.
[63] Evans M-H, Richardson AD, Wang L, Wood RJK. Effect of hydrogen on butterfly and white etching crack (WEC) formation under rolling contact fatigue (RCF). Wear 2013;306:226–41.
[64] Kordestani M, Rezamand M, Orchard M, Carriveau R, Ting DSK, Saif M. Planetary gear faults detection in wind turbine gearbox based on a ten years historical data from three wind farms. IFAC Pap 2020:6.
[65] Lewis, M., 2018, "Micro-Pitting of Wind Turbine Bearings - a Review," LinkedIn Pulse [Online]. Available: https://www.linkedin.com/pulse/micro-pitting-wind-turbine-bearings-review-mike-lewis/. [Accessed: 08-Sep-2022].
[66] Schröder T, Jacobs G, Rolink A, Bosse D. FlexPad' - innovative conical sliding bearing for the main shaft of wind turbines. J Phys: Conf Ser 2019:11.
[67] Rolink A, Jacobs G, Schröder T, Keller D, Jakobs T, Bosse D, et al. Methodology for the systematic design of conical plain bearings for use as main bearings in wind turbines. Forsch Im Ing 2021;85(2):629–37.